

# Carrier dynamics in ion-implanted GaAs studied by simulation and observation of terahertz emission

J. Lloyd-Hughes,<sup>1,\*</sup> E. Castro-Camus,<sup>1</sup> M.D. Fraser,<sup>2</sup> C. Jagadish,<sup>2</sup> and M.B. Johnston<sup>1</sup>

<sup>1</sup>*Department of Physics, University of Oxford, Clarendon Laboratory, Parks Road, Oxford, OX1 3PU, United Kingdom*

<sup>2</sup>*Department of Electronic Materials Engineering, Research School of Physical Sciences and Engineering, Institute of Advanced Studies, Australian National University, Canberra ACT 0200, Australia*

(Received 23 July 2004; Published 22 December 2004)

We have studied terahertz (THz) emission from arsenic-ion implanted GaAs both experimentally and using a three-dimensional carrier dynamics simulation. A uniform density of vacancies was formed over the optical absorption depth of bulk GaAs samples by performing multi-energy implantations of arsenic ions (1 and 2.4 MeV) and subsequent thermal annealing. In a series of THz emission experiments the frequency of peak THz power was found to increase significantly from 1.4 to 2.2 THz when the ion implantation dose was increased from  $10^{13}$  to  $10^{16}$  cm<sup>-3</sup>. We used a semi-classical Monte-Carlo simulation of ultra-fast carrier dynamics to reproduce and explain these results. The effect of the ion-induced damage was included in the simulation by considering carrier scattering at neutral and charged impurities, as well as carrier trapping at defect sites. Higher vacancy concentrations and shorter carrier trapping times both contributed to shorter simulated THz pulses, the latter being more important over experimentally realistic parameter ranges.

PACS numbers: 78.47.+p, 78.20.Bh, 61.72.Vv, 68.55.Ln

DOI: 10.1103/PhysRevB.70.235330

## I. INTRODUCTION

The technique of terahertz time-domain spectroscopy (THz-TDS) has seen wide application in recent years. By resolving carrier dynamics on ultra-short time scales THz-TDS has proven invaluable in areas of physics as disparate as investigating the energy gap in high  $T_c$  superconductors<sup>1</sup>, determining low-energy vibrational modes in oligomers<sup>2</sup>, and observing the onset of quasi-particle screening in GaAs<sup>3</sup>.

Such studies have become possible through the development of large bandwidth, high power THz emission sources based on the ultra-fast separation of photoexcited carriers in semiconductors. The resulting change in current produces an electromagnetic transient, typically a single or half-cycle pulse, with a broad spectrum covering THz frequencies. Charge separation can be the result of differing electron and hole mobilities (the photo-Dember effect), or alternatively may result from an electric field accelerating electrons and holes in opposite directions. In the later case, the electric field can be internal, such as the surface depletion field near a semiconductor surface, or externally applied as in a photoconductive switch (PCS). The study of surface emitters can help to elucidate aspects of ultra-fast carrier dynamics, such as the enhancement of THz emission under a magnetic field<sup>4,5,6</sup>, and the relative importance of the photo-Dember and surface field charge separation mechanisms in GaAs and InAs<sup>6,7</sup>. Additionally, surface emitters can produce the well-collimated THz beams<sup>8</sup> desirable for many THz imaging applications.

In the effort to improve THz emitters, one method for achieving a greater bandwidth is to shorten the electric field rise time, normally limited by the duration of the exciting infrared pulse. Another approach is to reduce the duration of the electric field transient after excitation by choosing a semiconductor with a short carrier lifetime, and/or a high momentum scattering rate. One suitable material is low-temperature-grown (or LT-) GaAs, in which As precipitates

and trapping centres result in a short ( $< 1$  ps) carrier lifetime, enabling THz emission extending to over 30 THz<sup>9</sup>. Alternatively the technique of ion implantation can be used, in which incident energetic ions damage the crystal structure of a semiconductor. The principal defect in arsenic ion-implanted GaAs (GaAs:As<sup>+</sup>) is thought to be the antisite donor defect As<sub>Ga</sub>, where As replaces Ga on some Ga lattice sites. Deep-level transient spectroscopy has found that the defect energy levels in GaAs:As<sup>+</sup> lay  $\sim 0.3$  eV below the conduction band<sup>10</sup>. Such deep-level defects can decrease THz pulse duration (increase THz bandwidth) by acting as carrier trapping and scattering centres, and result in carrier lifetimes of the order of 0.1 ps<sup>11,12</sup>.

The controllable ion dosage permits ion-implanted GaAs samples with reproducible properties, in contrast to LT-GaAs where the difficulty of temperature control results in samples with nominally the same growth parameters having varying properties. Ion-implantation has the further advantage of generating depth-dependent damage profiles (by choosing the ion type, dose, and energy) in specific sample areas. By performing a post-implant anneal the resistivity of GaAs:As<sup>+</sup> can be increased to levels comparable to LT-GaAs<sup>12,13</sup>, as required for photoconductive switches.

Both surface field<sup>14</sup> and photoconductive antenna<sup>15</sup> ion-implanted THz emitters have been previously studied, and were found to produce THz radiation at slightly higher frequencies than semi-insulating GaAs<sup>15</sup>. Additionally, ion-implanted photoconductive antennae have been used as detectors<sup>16</sup>, but no bandwidth improvement could be seen. These studies utilised low energy ions, typically 200 keV, resulting in implantation depths of only  $\sim 0.1$   $\mu$ m. However, as the infrared absorption depth is  $\sim 0.8$   $\mu$ m in GaAs only  $\sim 10\%$  of photocarriers are generated within this distance, and the non-implanted layer dominates THz emission.

In this paper we investigate GaAs implanted with dual, high energy (1 MeV and 2.4 MeV) As ion doses, creating an

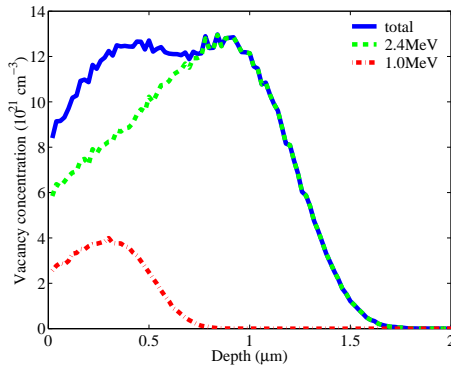


FIG. 1: (Colour online) Depth dependence of vacancies (including recoil vacancies) calculated using SRIM software<sup>17</sup> for the sample with highest ion dose. The 1 MeV,  $2.5 \times 10^{15} \text{ cm}^{-2}$  dose (dash-dotted line) and 2.4 MeV,  $1.0 \times 10^{16} \text{ cm}^{-2}$  dose (dashed line) create an approximately uniform damage profile (solid line) extending over  $1 \mu\text{m}$  from the surface. By scaling the concentration according to the dose, the distributions for lower dose samples can be obtained.

approximately uniform damage profile extending  $\sim 1 \mu\text{m}$  into the semiconductor. In Section II we describe the terahertz emission from samples irradiated with various ion doses, and discuss the effect of a post-implant thermal annealing step. Simulation results of THz emission from ion-implanted GaAs obtained from a three-dimensional carrier dynamics model<sup>6</sup> are presented in Section III.

## II. EXPERIMENT

The Australian National University 1.7 MV tandem accelerator was used to irradiate GaAs samples from the same ingot with  $\text{As}^+$  ions. By employing a two-stage implant of 1 MeV and 2.4 MeV (implanted at room temperature) an approximately uniform damage profile  $> 1 \mu\text{m}$  in depth was created (Fig. 1) in 7 samples at incident ion doses ranging from  $2.5 \times 10^{12} \text{ cm}^{-2}$  to  $2.5 \times 10^{15} \text{ cm}^{-2}$  (1 MeV implant) and  $1 \times 10^{13} \text{ cm}^{-2}$  to  $1 \times 10^{16} \text{ cm}^{-2}$  (2.4 MeV implant). A duplicate set of samples was produced that were annealed for 30 min. at  $500^\circ\text{C}$  under  $\text{AsH}_3$ . Calculations using the Stopping Range of Ions in Matter (SRIM) software<sup>17</sup> predict that the implanted ion concentration in the lowest dose sample is  $\sim 1 \times 10^{17} \text{ cm}^{-3}$ . Assuming that 99% of  $\text{As}_{\text{Ga}}$  antisites are instantly annealed<sup>17</sup> due to the implantation being performed at room temperature, we estimate an n-type doping concentration of  $\sim 1 \times 10^{15} \text{ cm}^{-3}$  for the lowest dose sample. Damage distributions were also calculated using SRIM, and verified using X-ray diffraction. Approximately 10,000 vacancies were found to be produced per  $\text{As}^+$  ion.

The surface field THz emission from each GaAs: $\text{As}^+$  sample was studied using THz-TDS. Infrared pulses from a mode-locked 10 fs Ti-sapphire laser ( $\lambda = 800 \text{ nm}$ ,  $\Delta\lambda = 135 \text{ nm}$ , 75 MHz repetition rate,  $\sim 400 \text{ mW}$  typical beam power) were incident on the sample at  $45^\circ$ . A lens focused the infrared pulses to a Gaussian beam-waist of  $\sigma = 90 \mu\text{m}$ . The sample was positioned  $\sim 1 \text{ cm}$  from the pump beam focus, with a Gaussian beam-waist of  $\sigma = 160 \mu\text{m}$  chosen to provide a

collimated THz beam<sup>8</sup>. The THz radiation was collected by an off-axis parabolic mirror placed at its focal length from the pump beam focus, and refocused by an identical mirror onto a  $0.2 \text{ mm}$  thick  $\langle 1\bar{1}0 \rangle$  ZnTe crystal. A delayed probe beam was split from the pump using a 10% beam-splitter, and also illuminated the ZnTe. The change in the probe's polarization was measured as a function of delay using an electro-optic sampling (EOS) system consisting of a Wollaston prism,  $\lambda/4$  waveplate and balanced photodiodes. The pump beam was chopped at  $\sim 1 \text{ kHz}$ , enabling the voltage across the detector to be measured by a lock-in amplifier (200 ms time constant), from which the THz electric field was calculated<sup>18</sup>. Following the procedure of Zhao *et al.*<sup>18</sup> we determine that our EOS system operates in the shot-noise limit, with a noise-equivalent THz electric field  $E_{\text{NEF}} \simeq 0.01 \text{ Vm}^{-1}$  consistent with the experimentally observed root-mean-square noise  $E_{\text{RMS}} \simeq 0.01 \rightarrow 0.02 \text{ Vm}^{-1}$ .

The THz electric field emitted by each of the 7 annealed samples was thus measured, with signal-to-noise ratios of above 150:1. The maximum THz electric field  $E_{\text{THz}}^{\text{max}}$  was of the order of  $3 \text{ Vm}^{-1}$ , less than we observe for our unimplanted GaAs reference sample ( $4 \text{ Vm}^{-1}$ ), and an InAs sample ( $216 \text{ Vm}^{-1}$ ) with the same experimental setup. For comparison, the maximum THz electric field strength reported in the literature from a photoconductive antenna is  $9500 \text{ Vm}^{-1}$  (Ref. 18).  $E_{\text{THz}}^{\text{max}}$  was not found to vary systematically with ion dose, perhaps because of variations in the surface potential of the samples, which can greatly alter the surface field strength.

Typical THz electric fields are shown in Fig. 2 for low ( $2.5 \times 10^{12} \text{ cm}^{-2}$  at 1 MeV,  $1 \times 10^{13} \text{ cm}^{-2}$  at 2.4 MeV) and high ( $1.25 \times 10^{15} \text{ cm}^{-2}$  at 1 MeV,  $5 \times 10^{15} \text{ cm}^{-2}$  at 2.4 MeV) implant doses. At higher implant doses we observe that the THz pulse duration is shorter, and that the negative peak after the principal peak has both larger magnitude and smaller period (Fig. 2(a)). In Fig. 2(b) the Fourier transforms of the time-domain electric field show that at greater ion doses THz emission shifts to higher frequencies.

The post-implant thermal annealing step ( $500^\circ\text{C}$ , 30 min.) was observed to result in larger peak THz fields, and greater power at low frequencies, as shown in Fig. 3 for the lowest dose sample ( $n_d = 2.5 \times 10^{12} \text{ cm}^{-2}$  at 1 MeV,  $n_d = 2.5 \times 10^{12} \text{ cm}^{-2}$  at 2.4 MeV). Annealing removes defects, at least partly repairing the damaged crystal structure. Because defects scatter carriers, and can also trap conduction band electrons, we can qualitatively predict that annealing will increase the pulse width, decreasing the relative THz emission at high frequencies.

## III. SIMULATION

In order to model the ultra-fast carrier dynamics leading to terahertz emission from semiconductor surfaces in such a way that reproduces the experimentally observed features it is appropriate to employ a three-dimensional Monte Carlo simulation, such as presented in Ref. 6. This model included the interactions between extrinsic and photogenerated carriers in  $\Gamma$  and  $L$ -valleys, plasmon and magnetoplasmon effects, and the dielectric-air interface, and has been used to distinguish between the diffusion (photo-Dember) and surface field

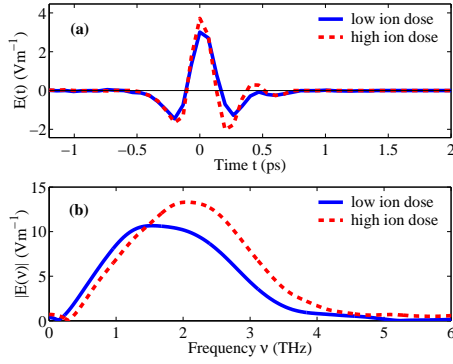


FIG. 2: (Colour online) Measured THz electric field  $E_{\text{THz}}$  emitted via the surface field mechanism from GaAs:As<sup>+</sup> samples implanted with low doses (solid lines,  $1 \times 10^{13} \text{ cm}^{-2}$  at 2.4 MeV and  $2.5 \times 10^{12} \text{ cm}^{-2}$  at 1 MeV) and high doses (dotted lines,  $5 \times 10^{15} \text{ cm}^{-2}$  at 2.4 MeV and  $1.25 \times 10^{15} \text{ cm}^{-2}$  at 1 MeV). The time and frequency domain THz electric fields are shown in (a) and (b). The peak electric fields and trailing negative peaks are  $+3.0, -1.5 \text{ V m}^{-1}$  and  $+3.7, -2.0 \text{ V m}^{-1}$  for the low and high dose samples respectively.

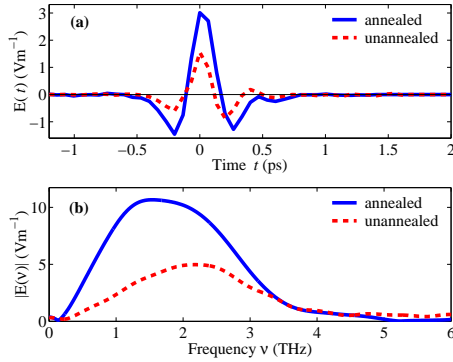


FIG. 3: (Colour online) THz emission from unannealed (dotted lines) and annealed GaAs:As<sup>+</sup> (solid lines) for the lowest implant dose ( $1 \times 10^{13} \text{ cm}^{-2}$  at 2.4 MeV and  $2.5 \times 10^{12} \text{ cm}^{-2}$  at 1 MeV). Annealing causes an increase in maximum THz field from  $1.6 \text{ V m}^{-1}$  (unannealed) to  $3.0 \text{ V m}^{-1}$  (annealed), but a decrease in the frequency of peak power from 2.1 THz (unannealed) to 1.6 THz (annealed).

mechanisms of charge separation in InAs and GaAs<sup>6,8</sup>, and to provide a quantitative explanation of the enhancement of THz emission under a magnetic field<sup>6</sup>.

In this section we present simulations of the THz emission from GaAs:As<sup>+</sup> using a version of the model of Ref. 6, extended to include the effects of the significant concentrations of vacancies and trapping defects. All simulations used the physical properties of GaAs as given in Table 1 of Ref. 6, and the laser parameters of Sec. II. Defect concentrations were assumed to be uniform over the range of infrared absorption, as is approximately the case in Fig. 1. Altering the charged impurity (donor) concentration was not found to significantly alter the spectral shape of THz emission.

## A. Neutral impurity scattering

When As<sup>+</sup> ions collide with atoms in GaAs both the incident ion and the recoiling target atoms introduce vacancies, which act as carrier scattering centres. Calculations using SRIM<sup>17</sup> suggest that approximately 10,000 vacancies are produced per incident ion, with the damage profile of Fig. 1. For our unannealed samples this corresponds to vacancy concentrations ranging from  $N_{\text{vac}} \sim 10^{19} \text{ cm}^{-3}$  to  $\sim 10^{22} \text{ cm}^{-3}$ . Electron paramagnetic resonance experiments have shown<sup>19</sup> that the concentration of arsenic antisite defects is about  $10^{18} \text{ cm}^{-3}$  after a 500°C, 30 min. anneal, for ion doses of  $10^{16} \text{ cm}^{-2}$ . Since  $N_{\text{vac}}$  for our annealed samples therefore varies from  $10^{15} \text{ cm}^{-3}$  to  $10^{18} \text{ cm}^{-3}$ , carrier-vacancy scattering cannot be disregarded as it normally is at lower defect concentrations.

Vacancies are included in the simulation by assuming that carriers scatter elastically from an electrically neutral spherical square well of width  $R$ , as defined by the potential  $V = -V_0$  for carrier-vacancy distances  $r \leq R$  and  $V = 0$  for  $r > R$ . Following the partial-wave approach taken in Ref. 20, the momentum scattering rate  $W_{\text{vac}}$  can be calculated from the  $l = 0$  wave cross-section  $\sigma$  using  $W_{\text{vac}} = \sigma N_{\text{vac}} v$ , where  $v$  is the electron velocity before (and after) scattering. The resulting expression is:

$$W_{\text{vac}} = \frac{4\pi\hbar N_{\text{vac}}}{m^*k} \frac{(k \cot kR - \alpha \cot \alpha R)^2}{(k^2 + \alpha^2 \cot^2 \alpha R)(1 + \cot^2 kR)} \quad (1)$$

where  $\alpha$  is given by:

$$\alpha = \sqrt{\frac{2m^*(E + V_0)}{\hbar^2}} \quad (2)$$

The final state carrier is scattered uniformly into  $4\pi$  steradians, because of the spherical symmetry of the well. Taking the values of  $R = 3 \text{ nm}$  and  $V_0 = 300 \text{ meV}$ <sup>10</sup> produces a scattering rate ranging from  $\sim 10^{11} \text{ s}^{-1}$  at  $N_{\text{vac}} = 1 \times 10^{15} \text{ cm}^{-3}$  to  $\sim 10^{14} \text{ s}^{-1}$  at  $N_{\text{vac}} = 1 \times 10^{18} \text{ cm}^{-3}$ .

To enable a comparison between these momentum scattering rates and those from mechanisms previously included in the simulation, we plot in Fig. 4 the average momentum scattering rates of electrons in the  $\Gamma$ -valley as a function of time  $t$  after the infrared pulse for  $N_d, N_{\text{vac}} = 1 \times 10^{15} \text{ cm}^{-3}$ . The scattering rates after  $t = 0 \text{ ps}$  are averaged over all photoinjected and extrinsic electrons, whereas before the infrared pulse arrives only extrinsic electrons contribute. The time dependence of the scattering rates is a consequence of the evolution of the carrier energy and concentration distributions. The greatest contributions to the total rate are attributed to electron-hole scattering and charged impurities, which both decrease at  $t = 0$  since they are inversely proportional to the local carrier density<sup>6</sup>. LO-phonon emission and absorption and TO-phonon emission and absorption followed by a jump into the L-valley initially contribute  $\sim 10\%$  of the total rate, but become less significant at later times when the average carrier energy has decreased. Acoustic phonon and neutral vacancy scattering provide only  $\sim 1\%$  of the total rate.

While Fig. 4 provides some insight into the significance of the various momentum scattering mechanisms, the angular distribution of each mechanism must also be considered. At  $N_{\text{vac}} = 1 \times 10^{17} \text{ cm}^{-3}$  the vacancy scattering rate is  $\sim 6 \times$

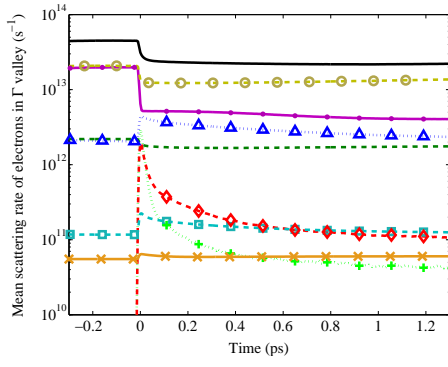


FIG. 4: (Colour online) Momentum scattering rates for electrons in the  $\Gamma$ -valley, with donor and vacancy concentrations of  $1 \times 10^{15} \text{ cm}^{-3}$  each. The rate for each scattering mechanism is averaged over all particles in the simulation, and is plotted as a function of time after laser excitation. The largest contributions to the total rate (solid line) come from electron-hole scattering (circles) and charged impurity scattering (dots). LO-phonon emission (triangles) and absorption (dashed line) are also significant. Acoustic phonon scattering (squares) and vacancy scattering (diagonal crosses) produce lower rates. Least important are TO-phonon absorption (diamonds) and emission (vertical crosses), where in both cases the electronic final state is in the L-valley. The infrared pulse arrives at  $t = 0$  ps, and produces a step in most scattering rates.

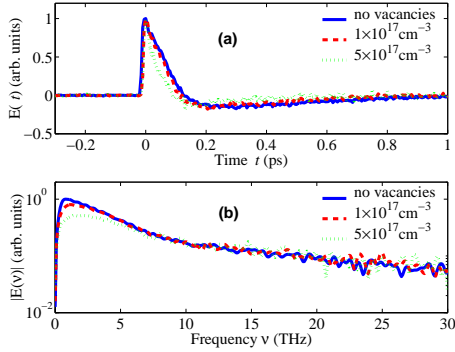


FIG. 5: (Colour online) Simulated THz emission in (a) the time domain and (b) the frequency domain with no vacancies, and for vacancy concentrations of  $1 \times 10^{17} \text{ cm}^{-3}$ ,  $5 \times 10^{17} \text{ cm}^{-3}$ . The FWHM of the spectra increase with vacancy concentration. Coherent phonon oscillations<sup>21</sup> are not observed because the response of the crystal lattice is not included in the simulation.

$10^{13} \text{ s}^{-1}$ , i.e. only 10% of the total rate, yet as can be seen in Fig. 5(a) the THz pulse duration is reduced. This is a consequence of the uniform angular distribution for vacancy scattering: the carrier direction is altered more significantly than in the other mechanisms.

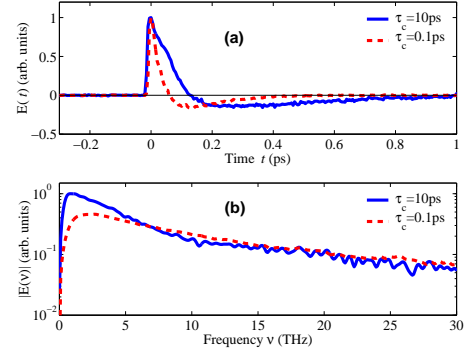


FIG. 6: (Colour online) Simulated THz electric field from bulk GaAs at carrier trapping times of  $\tau_c = 10$  ps and  $\tau_c = 0.1$  ps. In (a) the unfiltered simulated  $\tau_c = 0.1$  ps pulse (dashed line) has shorter duration than the 10 ps (solid line). Their Fourier transforms are shown in (b).

## B. Carrier-trapping defects

The effect of trapping defects on THz emission was included in our model by introducing an exponential decay of the number of photoexcited carriers  $n$  as a function of time  $t$  after the infrared pulse according to the equation:

$$n(t) = n(0)e^{-t/\tau_c} \quad (3)$$

where  $\tau_c$  is the carrier trapping lifetime. Time-resolved photoluminescence experiments of GaAs:As<sup>+</sup> implanted with a single  $10^{16} \text{ cm}^{-2}$  dose of 2 MeV ions have measured the carrier trapping time to be as short as  $\tau_c = 0.1$  ps<sup>11,12</sup>. It is important to distinguish  $\tau_c$  from the carrier recombination time, which is  $\sim 4$  ps<sup>22</sup>. We assume that once trapped, carriers cannot escape the defect via thermal excitation, and that trapped carriers do not alter free carrier states. When the number of carriers  $n$  is reduced on time scales of  $< 1$  ps the electric field decay time after the pulse can be shortened, as shown in Fig. 6, resulting in a greater bandwidth. At  $\tau_c = 0.1$  ps the FWHM from the simulation is 7.8 THz, nearly 80% larger than at a carrier trapping time of 100 ps (FWHM = 4.4 THz).

## IV. COMPARISON OF EXPERIMENT AND SIMULATION

The spectrum of the simulated THz emission has a larger magnitude at both low and high frequencies than the experimental data (Fig. 7(b)). This can be accounted for by the effect of the EOS system and the parabolic mirrors used to collect the THz radiation. A frequency-domain picture of EOS with ZnTe has been presented by Gallot *et al.*<sup>23,24</sup> that models the effect of the detection apparatus using three complex filters, namely: the spectrum of the autocorrelation of infrared pulse (which has negligible effect), the frequency-dependent electro-optic susceptibility  $\chi^{(2)}$  of ZnTe, and the mismatch between the infrared group velocity and THz phase velocity in ZnTe. The resulting low-pass filter causes the high frequency components to reduce in magnitude, as shown in Fig. 7(b). While the slow drop-off in simulated electric field at

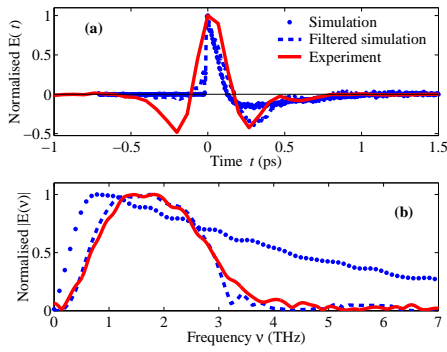


FIG. 7: (Colour online) Comparison of simulated THz emission from GaAs with n-type doping  $N_d = 1 \times 10^{15} \text{ cm}^{-3}$  using the low-dose sample data from Fig. 2. In (a) the simulated electric field (dots) is seen to have a sharp rise  $\sim 10$  fs in duration, and to drop sharply after  $\sim 0.1$  ps, producing the broad spectrum in (b). When low-pass and high-pass filters are applied (taking account of the dispersion in ZnTe, and diffraction-limited collection respectively, as described in the text), the filtered spectrum (dashed line) can be seen to match the experimental spectrum (solid) extremely well. When transformed back into the time-domain, the filtered simulated electric field (dashed line of (a)) matches for times  $\gtrsim 0.2$  ps.

increasing frequencies suggests that large bandwidths are possible from surface field THz emitters, experimentally a thin ( $\sim 10 \mu\text{m}$ ) ZnTe crystal is necessary to observe such frequency components, which would result in a prohibitively small signal.

While the experiment was designed to collect THz radiation with high efficiency, low frequency THz radiation emitted from the sample surface will be diffracted beyond the collection capability of the parabolic mirrors. By treating the two parabolic mirrors as a single thin lens, Côté *et al.* have calculated the high-pass filter corresponding to this effect<sup>25</sup>. They found that the approximate filter function  $F_{\text{high}}(\omega) = \text{erf}^2(2\omega R\sigma/cf)$ , where the THz radiation has a Gaussian beam-waist  $\sigma$ , and is collected by two parabolic mirrors each of focal length  $f$  and radius  $R$ . For our experimental geometry ( $f = 15$  cm,  $R = 2.5$  cm,  $\sigma = 0.16$  mm) this filter has a steep rise from 0 to 1 between 0 and  $\sim 1.5$  THz, which when applied to the simulated data causes a reduction in low frequency components of the electric field.

Multiplying the simulated spectrum by these filters in the frequency domain produces a high accuracy match to the experimental spectra (Fig. 7(b)). Taking the inverse Fourier transform of the filtered simulated spectrum results in a time-domain trace that compares adequately with the experimental time-domain data (Fig. 7(a)). The low-pass (ZnTe) filter causes an increase both in the oscillation period and in the negative peak amplitude after the pulse. The dip in experimental electric field before the pulse is not reproduced by the application of the filters to the simulated data.

The filters were applied to simulated spectra at carrier trapping times varying from  $\tau_c = 0.1$  ps to  $\tau_c = 100$  ps. As shown in Fig. 8, this enables a direct comparison between the experimental  $f_{\text{peak}}$  as a function of ion dose, and  $f_{\text{peak}}$  extracted from the model as a function of  $1/\tau_c$ . When  $\tau_c = 0.1$  ps

the filtered spectral peak is at 2.1 THz, in excellent agreement with the value (2.2 THz) of the highest dose sample ( $2.5 \times 10^{15} \text{ cm}^{-2}$  at 1 MeV,  $1 \times 10^{16} \text{ cm}^{-2}$  at 2.4 MeV). As the carrier trapping time is increased ( $1/\tau_c$  decreased) the simulation tends to  $f_{\text{peak}} = 1.6$  THz, in agreement with the experimental value. Values of the FWHM of filtered simulated spectra are approximately independent of  $\tau_c$ , owing to the bandwidth limitations imposed by the 0.2 mm-thick ZnTe crystal.

A smaller increase in  $f_{\text{peak}}$  was observed over the experimental range of vacancy concentrations: at  $10^{15} \text{ cm}^{-3}$   $f_{\text{peak}} = 1.6$  THz, and at  $10^{18} \text{ cm}^{-3}$   $f_{\text{peak}} = 1.9$  THz. This suggests that carrier trapping may be more significant than carrier-vacancy momentum scattering in determining THz pulse duration.

The experimental reduction in the spectral peak of THz emission after annealing (Fig. 3) may be attributed to a combination of a reduction in carrier-vacancy scattering and an increase in carrier trapping time from  $\tau_c \sim 0.1$  ps to  $\tau_c \sim 1$  ps.

## V. CONCLUSION

We have studied the surface field THz emission from GaAs implanted with multiple doses of high energy arsenic ions both experimentally and via a three-dimensional carrier dynamics simulation. The effect of trapping defects and neutral impu-

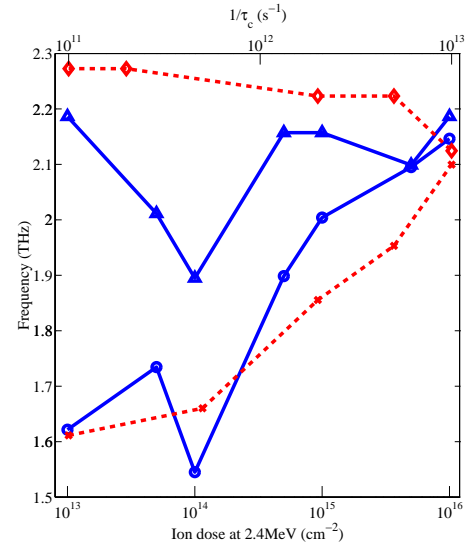


FIG. 8: (Colour online) Frequency of peak emitted THz power  $f_p$  (circles, solid line) and FWHM of spectra (triangles, solid line) as a function of ion dose at 2.4 MeV (the 1 MeV ion dose was a quarter of the 2.4 MeV dose).  $f_p$  is defined as the midpoint of the two frequencies at which the amplitude of the Fourier transform of the electric field is 95% of its maximum. The experimental data can be compared with values extracted from spectra produced by our carrier dynamics simulation (dashed lines), plotted as a function of inverse carrier trapping time  $1/\tau_c$ . The trend in  $f_p$  (crosses) from the simulation reproduces the experiment. The FWHM from the simulation (diamonds) do not vary with  $1/\tau_c$ , and are consistent with those measured.

rities on carrier dynamics was included in the model. At a short carrier trapping time of 0.1 ps our model predicts an increase in the FWHM of THz emission of nearly 80% above the FWHM at long ( $> 10$  ps) trapping times. This bandwidth increase was experimentally observed as a shift in peak spectral power towards higher frequencies at greater ion implant doses. We anticipate similar bandwidth improvements for photoconductive switches made from our GaAs:As<sup>+</sup> samples, but with greater available THz power. The momentum scattering rate of carriers from vacancy defects was found to be  $\sim 10^{14}\text{s}^{-1}$ , comparable to that of the two dominant scattering mechanisms in unimplanted GaAs (electron-hole and carrier-charged impurity scattering), for the vacancy concentrations expected in the highest dose sample. While the THz pulse duration decreased at high vacancy concentration, carrier-vacancy scattering was not found to account for the full shift

in peak experimental spectral power. While the simulation parameters were chosen to correspond to our GaAs:As<sup>+</sup> samples, the model is applicable to LT-GaAs, in which arsenic antisites (As<sub>Ga</sub>) are also the dominant defect, and which has comparable trapping times.

## VI. ACKNOWLEDGEMENTS

We would like to thank the EPSRC and the Royal Society for funding this research. E.C. thanks CONACyT (Mexico) for a scholarship. M.D.F. and C.J. acknowledge financial support from the Australian Research Council. Dr H. Tan is gratefully thanked for help with the annealing experiments.

- 
- \* Electronic address: james.lloyd-hughes@physics.ox.ac.uk
- <sup>1</sup> R. A. Kaindl, M. A. Carnahan, J. Orenstein, D. S. Chemla, H. M. Christen, H.-Y. Zhai, M. Paranthaman, and D. H. Lowndes, *Phys. Rev. Lett.* **88**, 027003 (2002).
  - <sup>2</sup> M. B. Johnston, L. M. Herz, A. L. T. Khan, A. Köhler, A. G. Davies, and E. H. Linfield, *Chem. Phys. Lett.* **377**, 256 (2003).
  - <sup>3</sup> R. Huber, F. Tauser, A. Brodschelm, M. Bichler, G. Abstreiter, and A. Leitenstorfer, *Nature* **414**, 286 (2001).
  - <sup>4</sup> A. Corchia, R. McLaughlin, M. B. Johnston, D. M. Whittaker, D. D. Arnone, E. H. Linfield, A. G. Davies, and M. Pepper, *Phys. Rev. B* **64**, 205204 (2001).
  - <sup>5</sup> M. B. Johnston, D. M. Whittaker, A. Corchia, A. G. Davies, and E. H. Linfield, *J. Appl. Phys.* **91**, 2104 (2002).
  - <sup>6</sup> M. B. Johnston, D. M. Whittaker, A. Corchia, A. G. Davies, and E. H. Linfield, *Phys. Rev. B* **65**, 165301 (2002).
  - <sup>7</sup> J. N. Heyman, N. Coates, A. Reinhardt, and G. Strasser, *Appl. Phys. Lett.* **83**, 5476 (2003).
  - <sup>8</sup> M. B. Johnston, A. Dowd, R. Driver, A. G. Davies, and E. H. L. and D. M. Whittaker, *Semicond. Sci. Technol.* **19**, S449 (2004).
  - <sup>9</sup> Y. C. Shen, P. C. Upadhyaya, E. H. Linfield, H. E. Beere, and A. G. Davies, *Appl. Phys. Lett.* **83**, 3117 (2003).
  - <sup>10</sup> W.-C. Chen and C. S. Chang, *J. Appl. Phys.* **81**, 7295 (1997).
  - <sup>11</sup> A. Krotkus, S. Marcinkevicius, J. Jasinski, M. Kaminska, H. H. Tan, and C. Jagadish, *Appl. Phys. Lett.* **66**, 3304 (1995).
  - <sup>12</sup> S. Marcinkevicius, C. Jagadish, H. H. Tan, M. Kaminska, K. Korona, R. Adomavicius, and A. Krotkus, *Appl. Phys. Lett.* **76**, 1306 (2000).
  - <sup>13</sup> G. R. Lin, W. C. Chen, C. S. Chang, S. C. Chao, K. H. Wu, T. M. Hsu, W. C. Lee, and C. L. Pan, *IEEE J. Quantum Electron.* **34**, 1740 (1998).
  - <sup>14</sup> G. R. Lin and C. L. Pan, *Appl. Phys. B: Lasers Opt.* **72**, 151 (2001).
  - <sup>15</sup> T.-A. Liu, M. Tani, and C.-L. Pan, *J. Appl. Phys.* **93**, 2996 (2003).
  - <sup>16</sup> T.-A. Liu, M. Tani, M. Nakajima, M. Hangyo, and C.-L. Pan, *Appl. Phys. Lett.* **83**, 1322 (2003).
  - <sup>17</sup> J. F. Ziegler and J. P. Biersack, available online at <http://www.srim.org>.
  - <sup>18</sup> G. Zhao, R. N. Schouten, N. van der Valk, W. T. Wenckebach, and P. C. M. Planken, *Review of Scientific Instruments* **73**, 1715 (2002).
  - <sup>19</sup> M. Kaminska, E. R. Weber, and C. Jagadish, *Proceedings of the 8th Conference on Semi-insulating III-IV Materials* (1994).
  - <sup>20</sup> B. K. Ridley, *Quantum Processes in Semiconductors* (Clarendon Press, Oxford, 1999), chap. 4.3.
  - <sup>21</sup> G. C. Cho, W. Kutt, and H. Kurz, *Phys. Rev. Lett.* **65**, 764 (1990).
  - <sup>22</sup> L. Giniunas, R. Danielius, H. H. Tan, C. Jagadish, R. Adomavicius, and A. Krotkus, *Appl. Phys. Lett.* **78**, 1667 (2001).
  - <sup>23</sup> G. Gallot, J. Zhang, R. W. McGowan, T.-I. Jeon, and D. Grischkowsky, *Appl. Phys. Lett.* **74**, 3450 (1999).
  - <sup>24</sup> G. Gallot and D. Grischkowsky, *J. Opt. Soc. Am. B* **16**, 1204 (1999).
  - <sup>25</sup> D. Côté, J. E. Sipe, and H. M. van Driel, *J. Opt. Soc. Am. B* **20**, 1374 (2003).